Nano Research

ISSN 1998-0124 CN 11-5974/O4
https://doi.org/10.1007/s12274-019-2543-0

Research Article

Unexpected intercalation-dominated potassium storage in WS_2 as a potassium-ion battery anode

Yuhan Wu[1], Yang Xu[2] (✉), Yueliang Li[3], Pengbo Lyu[4], Jin Wen[5], Chenglin Zhang[1], Min Zhou[1], Yaoguo Fang[1], Huaping Zhao[1], Ute Kaiser[3], and Yong Lei[1] (✉)

[1] *Fachgebiet Angewandte Nanophysik, Institut für Physik & ZMN MacroNano (ZIK), Technische Universität Ilmenau, Ilmenau 98693, Germany*
[2] *Department of Chemistry, University College London, London WC1H 0AJ, UK*
[3] *Central Facility for Electron Microscopy, Electron Microscopy Group of Materials Science, Ulm University, Ulm 89081, Germany*
[4] *Department of Physical and Macromolecular Chemistry, Faculty of Science, Charles University, 12843 Prague 2, Czech Republic*
[5] *Institute of Organic Chemistry and Biochemistry, Academy of Sciences of the Czech Republic, 16610 Prague 6, Czech Republic*

Received: 14 August 2019 / **Revised:** 1 October 2019 / **Accepted:** 12 October 2019

ABSTRACT

Unexpected intercalation-dominated process is observed during K^+ insertion in WS_2 in a voltage range of 0.01–3.0 V. This is different from the previously reported two-dimensional (2D) transition metal dichalcogenides that undergo a conversion reaction in a low voltage range when used as anodes in potassium-ion batteries. Charge/discharge processes in the K and Na cells are studied in parallel to demonstrate the different ion storage mechanisms. The Na^+ storage proceeds through intercalation and conversion reactions while the K^+ storage is governed by an intercalation reaction. Owing to the reversible K^+ intercalation in the van der Waals gaps, the WS_2 anode exhibits a low decay rate of 0.07% per cycle, delivering a capacity of 103 mAh·g^{-1} after 100 cycles at 100 mA·g^{-1}. It maintains 57% capacity at 800 mA·g^{-1} and shows stable cyclability up to 400 cycles at 500 mA·g^{-1}. Kinetics study proves the facilitation of K^+ transport is derived from the intercalation-dominated mechanism. Furthermore, the mechanism is verified by the density functional theory (DFT) calculations, showing that the progressive expansion of the interlayer space can account for the observed results.

KEYWORDS

potassium-ion battery, anode, WS_2, intercalation

1 Introduction

Research on sodium-ion and potassium-ion batteries (SIBs and PIBs) has been rapidly increasing since the late 2000s to examine their feasibility to serve as the alternatives of lithium-ion batteries (LIBs) [1–8]. One may argue that the theoretical capacity of a metallic Li anode is 3,861 mAh·g^{-1}, which is much larger than those of Na and K anodes (1,166 and 685 mAh·g^{-1}, respectively) [1]. However, the value is that of lithium rather than a Li anode because a battery cannot consume all the anode; these theoretical values are misinterpreted because anodes release the charge carrier during the battery process, but they cannot be fully transformed into the charge carrier [5, 9]. Recently, the theoretical capacities of different battery systems were estimated and compared with respect to the weight of various components in a 18,650 battery that is currently among the most common types of LIBs [9]. The comparison has shown that the specific energy/energy density of a SIB or a PIB is only 20% lower than that of a LIB, and SIBs have no considerable advantage over PIBs in terms of the specific energy. This highlights the promise of the commercial development of PIBs, and as a result, it is of utmost importance to explore new electrode materials for this exciting class of batteries.

Two-dimensional transition metal dichalcogenides (2D TMDs) have a unique layered structure characterized by weak interlayer van der Waals interaction and strong intralayer covalent bonding. The structure allows the intercalation of guest species in the interlayer space and naturally provides perfect 2D diffusion pathways. 2D TMDs have shown impressive properties in a broad range of applications for decades, for instance, the flagship of the material family, MoS_2 [10]. Because the tendency for the formation of a 2D structure pillared by van der Waals forces is more for heavier elements, growing attention has been paid to 2D tungsten dichalcogenides recently [11–14]. Considering that the industrial consumption of Mo is currently higher while having a lower amount of mineral resources, W, with a similar natural abundance as Mo [15], is commercially more favourable for industrial applications.

In the field of PIBs, various 2D TMDs, including sulphides (MoS_2 [16], SnS_2 [17], VS_2 [18], and ReS_2 [19]) and selenides ($MoSe_2$ [20] and VSe_2 [21]), have been studied as potential anode materials, but little has been done to explore tungsten dichalcogenides in this regard. The reported studies have demonstrated high capacities derived from the conversion reaction, i.e., the reduction of transition metals at a low voltage, that destroys the 2D diffusion pathways; while limiting discharge depth to 0.5 V seems to be able to maintain the pathways as intercalation reaction replaces conversion reaction to store K^+ [22, 23], but there is a penalty of energy density of full-cells due to the cut-off voltage. Based on the intrinsically structural similarity, it is natural to expect that 2D tungsten dichalcogenides would show a similar behavior of storing K^+ and face the same dilemma. However, it could also be misleading, as essential differences can be obscured when interpreting the behavior of one 2D TMD by a mechanism proposed for other TMDs. Therefore, it is highly

Address correspondence to Yong Lei, yong.lei@tu-ilmenau.de; Yang Xu, y.xu.1@ucl.ac.uk

beneficial to investigate the K^+ storage in 2D tungsten dichalcogenides.

Herein, we investigated commercial WS_2 and revealed its intercalation-dominated K^+ storage in the full discharge voltage window to 0.01 V (vs. K^+/K). By comparing the charge/discharge processes of WS_2 in SIBs and PIBs, we showed that the Na^+ storage in WS_2 follows the well-recognized path, i.e., a conversion reaction at the high voltage range followed by an intercalation reaction at the low voltage range, while the K^+ storage in WS_2 is governed by the intercalation reaction rather than the conversion reaction. The mechanism was verified by the density functional theory (DFT) calculations. Owing to the highly reversible intercalation, WS_2 exhibited a low capacity decay rate of 0.07% per cycle at 100 $mA{\cdot}g^{-1}$, capacity retention of 57% when the rate increased from 50 to 800 $mA{\cdot}g^{-1}$, and long-term stability at 500 $mA{\cdot}g^{-1}$. To the best of our knowledge, it is the first report of 2D TMDs that undergo such an unexpected electrochemical mechanism in PIBs at the applied condition.

2 Results and discussion

Commercial WS_2 powders were used as received, and the experimental details can be found in the Electronic Supplementary Material (ESM). The powders can be well assigned to 2H phase (JCPDS 08-0237, Fig. S1 in the ESM) with an interlayer spacing of 6.2 Å. Scanning electron microscopy (SEM) images (Fig. S2 in the ESM) show a plate-like morphology with a size being 2–5 μm and a thickness being 150–180 nm. We tested the powders against K and Na in the range of 0.01–3.0 V at 25 $mA{\cdot}g^{-1}$ and observed significantly different ion storage mechanisms. In the Na cell (Fig. 1(b)), Cycle1 discharge displays two well-defined plateaus at 0.6 and 0.25 V that correspond to the intercalation and conversion processes during the Na insertion, respectively [24, 25], delivering an initial capacity of 649 $mAh{\cdot}g^{-1}$. In contrast, in the K cell (Fig. 1(a)), Cycle1 discharge displays a quasi-plateau at 0.5 V and a slope towards 0.01 V. The absence of the low-voltage plateau indicates the conversion reaction may not take place during the K insertion, thereby delivering a lower capacity of 235 $mAh{\cdot}g^{-1}$. Cycle2 profile in the Na cell shifts to higher voltages (> 1.7 V), whereas Cycle2 discharge in the K cell remains below 0.8 V with a same shape of Cycle1. The two charge curves well overlap with each other, indicating good reversibility. Cyclic voltammetry (CV) curves of the two cells (Fig. S3 in the ESM) are in accordance with Figs. 1(a) and 1(b), respectively. Particularly, the strong contrast between the two sharp peaks (0.5 and 0.16 V) in the Na cell and one broad peak (0.46 V) in the K cell indicates the absence of the conversion reaction in the latter. We performed the XPS measurement on the electrodes after Cycle1 discharge. Surprisingly, W^0 peak was not detected in the case of the K cell (Fig. 1(c)) but clearly presented in the case of the Na cell with a bonding energy of 30.6 eV (Fig. S4 in the ESM), being significantly lower than those of the oxidized W [26]. The W^{x+} peak in Fig. 1(c) is attributed to the reduction of W^{4+} during the K insertion, while the W^{5+} peak is likely formed due to the air exposure before the measurement. This is even more significant in the Na cell, as the nanosized metal W has a high tendency to be oxidized, resulting in the formation of W^{6+} [17]. We noticed that a recent work reported the observation of the reduction of WS_2 to W below 0.08 V (vs. K^+/K), where there was no phase or structural characterization to show the presence of metallic W [27]. However, our XPS results clearly suggest the absence of the reduction upon K^+ intercalation. In addition, we observed the preservation of the WS_2 structure after the K^+ insertion by the high-resolution transmission electron microscopy (HRTEM) measurement (Figs. 1(d)–1(f)). The layered structure and clear lattice fringes of 0.27 nm that corresponds to the d spacing of the basal (100) plane can be seen at various areas that were characterized. The interlayer spacing is significantly expended up to 0.92 nm because of the K^+ insertion.

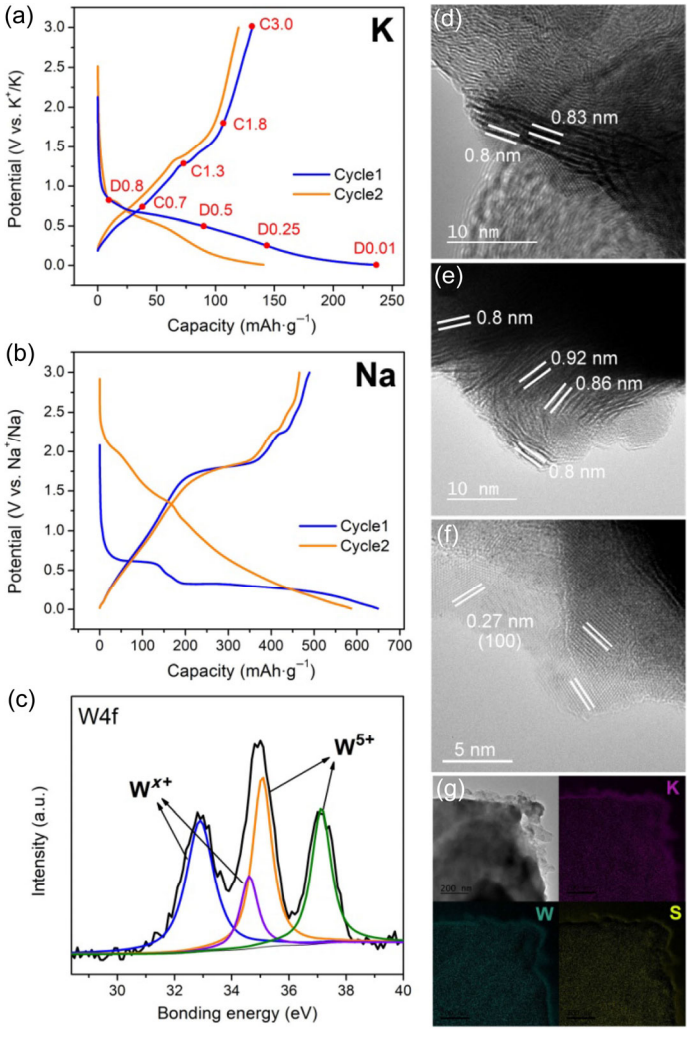

Figure 1 Charge/discharge profiles of the first two cycles of WS_2 in the K cell (a) and Na cell (b). W4f XPS spectrum (c), HRTEM images ((d)–(f)) and elemental mapping of WS_2 (g) in the K cell after the first discharge.

Elemental maps (Fig. 1(g)) acquired through the energy-filtered TEM [28] illustrates the even distribution of K, W and S. Therefore, the HRTEM observations once again suggest the K^+ storage in WS_2 is unexpectedly dominated by an intercalation process rather than a conversion process.

Owing to the minimal damage to the layered structure of WS_2, the intercalation-dominated K^+ storage should lead to stable cycle life and great rate capability. As expected, WS_2 delivered the capacities of 110.2 and 102.8 $mAh{\cdot}g^{-1}$ at 100 $mA{\cdot}g^{-1}$ after 2 and 100 cycles (Figs. 2(a) and 2(b)), respectively. It results in a very small decay of 0.07% per cycle, which as far as we know is the best cycling stability among all the intercalation-type PIB anodes [29–32]. The stabilized capacity (102.8 $mAh{\cdot}g^{-1}$) corresponds to 0.95 mol K^+ stored per formula, which is in a good agreement with the simulation results (will be shown in Fig. 5). The initial Columbic Efficiency (CE) 56% was relatively low, which is primarily caused by the formation of solid-electrolyte interface (SEI). With prolonging the cycles, the discharge plateau shifts to 0.8 V and the polarization between charge and discharge becomes smaller, which implies the K diffusion kinetics is improved, as will be proven by the electrochemical impedance spectroscopy (EIS) results in Fig. 4. As a result, CE increased to 96% after initial cycles. Rate capability is shown in Fig. 2(c). WS_2 delivered the capacities of 109, 99, 86, 74, 68 and 62 $mAh{\cdot}g^{-1}$ at the current densities of 50, 100, 200, 400, 600 and 800 $mAh{\cdot}g^{-1}$, respectively. It fully recovered to 112 $mAh{\cdot}g^{-1}$ when the current density was reduced back to 50 $mA{\cdot}g^{-1}$. Stable charge/discharge profiles can be

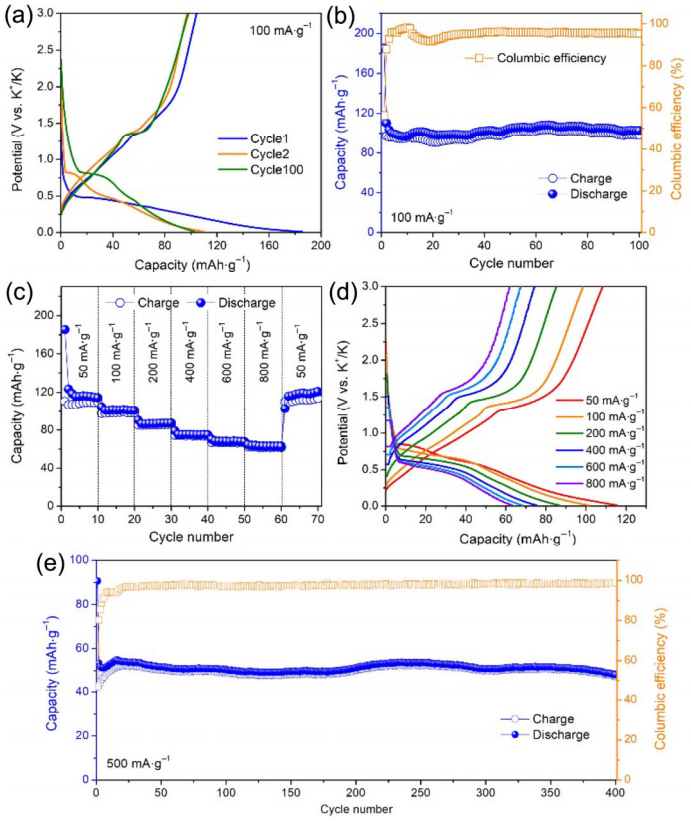

Figure 2 Charge/discharge profiles (a) and cycling performance of WS_2 (b) at 100 mA·g^{-1}. (c) Rate performance from 50 to 800 mA·g^{-1}. (d) Charge/discharge profiles at different current densities. (e) Cycling performance at 500 mA·g^{-1}.

seen at all testing current densities (Fig. 2(d)). The obtained rate capability shows the ability of WS_2 to fast insert and extract K^+ and is better than the intercalation-type titanate anodes [29–31]. Moreover, WS_2 exhibited great cycling stability at a high current density of 500 mAh·g^{-1}. It delivered 51.4 mAh·g^{-1} after 200 cycles and 48.2 mAh·g^{-1} after 400 cycles (Fig. 2(e)), which are 96% and 90% of the capacity at the 2nd cycle, respectively. Therefore, the long-term cycling stability and fast charge/discharge ability prove the suitability of WS_2 as an intercalation-type anode in PIBs. To validate this point, we assembled full-cells by using WS_2 and the intercalation-type Prussian blue cathode that was synthesized according to our previous work [33]. Figure S5(a) in the ESM shows the charge/discharge profiles of the full-cell at 100 mA·g^{-1}. The charging curve displays a semi-plateau around 3.2 V, while a slope was observed during discharging. The full-cell delivered Cycle2 discharge capacity of 109 mAh·g^{-1} and kept 60 mAh·g^{-1} after 50 cycles (Fig. S5(b) in the ESM).

We next analyzed the WS_2 electrodes during the first cycle to ascertain the proposed K^+ storage mechanism. Electrodes at different charge/discharge states (indicated in Fig. 1(a)) were subjected to the X-ray diffraction (XRD) and Raman spectroscopy measurements. A few conclusions can be drawn from a close observation of Fig. 3. First, the XRD patterns remain almost unchanged during the cycle, and sharp (002) and (004) peaks that are characteristic of the layered structure can be seen (Fig. 3(a)). This confirms the absence of conversion reaction as no W or K-S compounds was detected. Second, both (002) and (004) peaks gradually shift towards lower angles with increasing the discharge depth, indicating the gradual expansion of the interlayer spacing during the K^+ insertion, as previously shown in the HRTEM images. During charge, both peaks' positions remain unchanged (Fig. 3(b)), which suggests the interlayer spacing remains expanded even K^+ is extracted. A similar XRD pattern was obtained after the second discharge process (Fig. S6 in the ESM). Thus, these observations confirm that intercalation is the dominating process to store K^+ in WS_2. Third, Raman spectra at pristine and all cycled states (Figs. 3(c) and 3(d)) show two peaks located at 355.3 and 419.8 cm^{-1} that are attributed to the planar (E^1_{2g}) and out-of-plane (A_{1g}) vibration modes of WS_2, respectively [34]. This further demonstrates the K intercalation has minimal damage to the layered structure. WS_2 electrodes in the Na cell were subjected to the same measurements (Fig. S7 in the ESM). The layered structure sustained after an initial intercalation process (discharging to 0.4 V). It completely collapsed after the conversion process (discharging to 0.01 V), where only WO_3, Na_2O and Na_2S can be detected, and it cannot be restored after charge, being in accordance with the XPS results (Fig. S4 in the ESM). The E^1_{2g} and A_{1g} peaks in the Raman spectra disappear after discharging to 0.25 V and remain undetectable during the cycle. As a result, the Na cell exhibited fast capacity decay and retained 13% discharge capacity after only 30 cycles (Fig. S8 in the ESM), which is in sharp contrast with the cyclability in the K cell (Fig. 2(b)).

Several factors that might be possibly used to explain the observed K^+ storage mechanism in WS_2 should be ruled out. One factor to consider is that at deep discharge condition, there was not enough K^+ diffusion time to reach the conversion process. We ruled

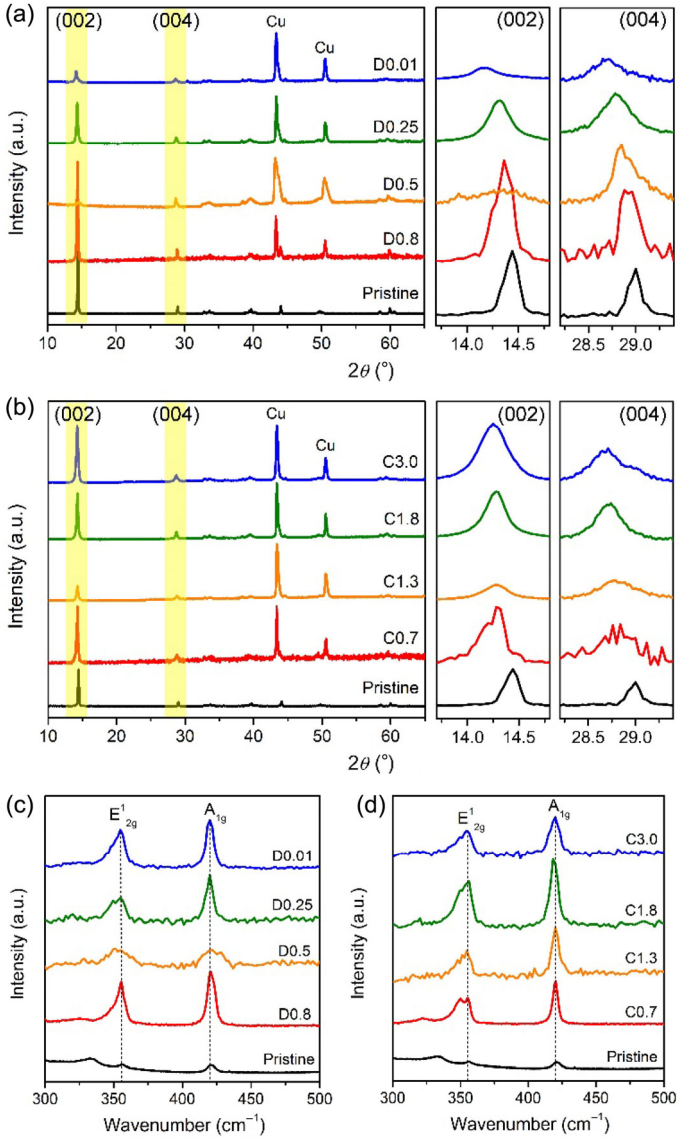

Figure 3 XRD patterns ((a) and (b)) and Raman spectra ((c) and (d)) of WS_2 in the K cell at different discharge ((a) and (c)) and charge states ((b) and (d)). The states are indicated in Fig. 1(a).

out this possibility by a control experiment where a WS_2 electrode was held at 0.01 V for 2 h at the end of the discharge. Both (002) and (004) peaks can be observed in the XRD pattern (Fig. S9 in the ESM). Another factor to consider is the size effect, which may cause kinetic difficulty of the K^+ diffusion. To examine this possibility, we synthesized a control sample with a small size. The XRD pattern of the sample (Fig. S10(b) in the ESM) can be indexed to the same structure of the commercial WS_2, and the significant peak broadening indicates the size has been greatly reduced. SEM image (Fig. S10(a) in the ESM) displays the diameter is below 200 nm and the protrusion of the surface is less than 10 nm. However, the discharge profile (Fig. S10(c) in the ESM) exhibits same features as those shown in Fig. 1(a), and no low-voltage plateau is observed, delivering a capacity that was even lower than that of the commercial powders (Fig. S10(d) in the ESM). Both (002) and (004) peaks can be found in the XRD pattern after the discharge (Fig. S10(b) in the ESM). In addition, we synthesized WS_2 nanosheets by directly exfoliating commercial WS_2 powders. The nanosheets are much smaller in lateral size (a few hundreds of nanometers) and much thinner (around tens of nanometers) compared to the commercial powders (Figs. S11(a) and S11(b) in the ESM). The nanosheets deliver a lower capacity than commercial powders at the same test condition (Fig. S11(c) in the ESM). Lastly, we tested commercial MoS_2 powders in a K cell, as it has an interlayer spacing (6.15 Å) that is close to that of WS_2. MoS_2 delivered three discharge plateaus at 1.1, 0.4 and 0.1 V (Fig. S12(a) in the ESM) that correspond to the sequential intercalation and conversion processes to store K [22]. As a result, the layered structure of MoS_2 collapsed and no peaks can be detected in the XRD patterns after initial discharge and charge (Fig. S12(b) in the ESM). Taken as a whole, the evidence supports that the intercalation-dominated K^+ storage mechanism we proposed is reasonable.

We further sought to understand the facilitation of the K^+ transport derived from the intercalation-dominated mechanism by using three electrochemical characterization techniques. First, CVs were tested in the range of 0.1–1 $mV{\cdot}s^{-1}$ (Fig. 4(a)). No shift of (de)intercalation peaks is observed with increasing the scan rate, which signals a minimal polarization of the intercalation reaction. According to the general expression of $i = av^b$, the b value is 0.5 for a semi-infinite linear diffusion-controlled process and close to 1.0 for a surface-controlled process [35, 36]. As shown in Fig. 4(b), a linear relationship can be observed, and the b values are determined to be 0.71 for the intercalation and 0.79 for the deintercalation. This suggests that solid-state diffusion is the rate-limiting factor and the intercalation reaction facilitates the K^+ diffusion in WS_2. Second, electrochemical galvanostatic intermittent titration (GITT) was used to evaluate the K^+ diffusion coefficient (D_k). Figure 4(c) shows the potential response during the intercalation and the value of D_k as a function of potential (calculation of D_k can be found in Fig. S13 in the ESM). The WS_2 electrode displays a progressively decreasing D_k with the potassiation proceeding towards 0.01 V, being 1.3×10^{-12} $cm^2{\cdot}s^{-1}$ at 0.86 V and 2.3×10^{-13} $cm^2{\cdot}s^{-1}$ at 0.27 V. It can be ascribed to the gradually increased repulsive charge from the occupied sites between the WS_2 slabs, which agrees with previous work [37–39]. Third, EIS was used to analyze the charge transfer kinetics. The Nyquist plots obtained after cycles are shown in Fig. 4(d) and were fitted using equivalent circuits to extract resistances (Fig. S14 and Table S1 in the ESM). The plots after cycle2 and cycle10 consist of two partially merged semi-circles that are attributed to the resistance related to solid-liquid interphase (SEI, R_{sei}) and charge transfer (R_{ct}) [40, 41]. Both resistances decrease from cycle2 (R_{sei}: 3,344 Ω; R_{ct}: 2,791 Ω) to cycle10 (R_{sei}: 2,074 Ω; R_{ct}: 2,044 Ω), indicating that the expansion of the interlayer spacing improves the K^+ transport. The two semicircles completely merged after cycle50 because of the similarity of the time constants of the two processes, and the overall interfacial resistance ($R_{int} = R_{sei} + R_{ct}$) that is represented by the diameter of the merged semicircle is calculated to be 1,833 Ω. This confirms the improved kinetic property of the intercalation reaction with prolonging the cycles [36]. Our kinetic study shows the intercalation-dominated storage mechanism favors the K^+ transport in the interlayer space, which results in the cycling stability shown in Fig. 2.

Moreover, we applied DFT calculations to verify the possibility of the intercalation-dominated K^+ storage. WS_2 bulk was first applied

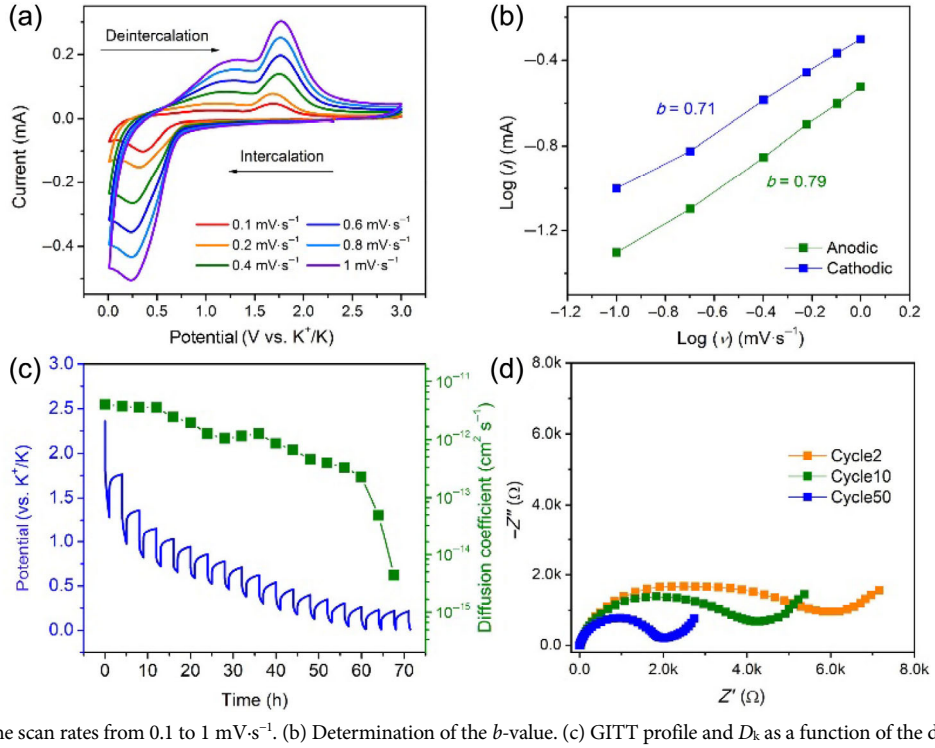

Figure 4 (a) CV curves at the scan rates from 0.1 to 1 $mV{\cdot}s^{-1}$. (b) Determination of the b-value. (c) GITT profile and D_k as a function of the discharge process. (d) Nyquist plots recorded after cycles.

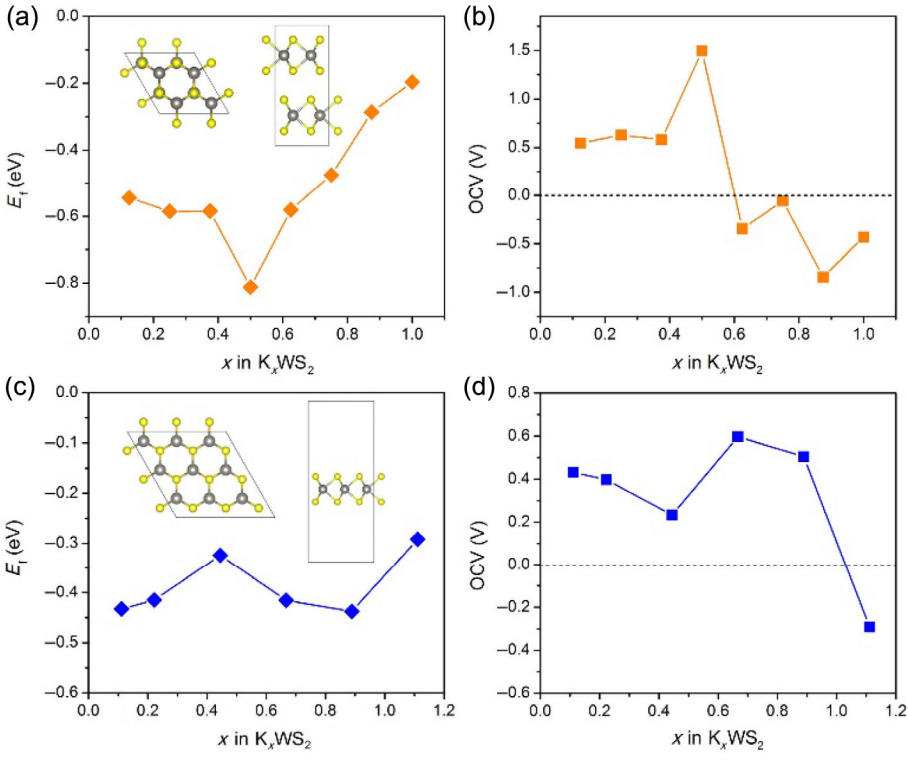

Figure 5 Formation energy ((a) and (c)) and OCV profiles ((b) and (d)) of x K-ions in bulk ((a) and (b)) and monolayer WS_2 ((c) and (d)). Insets in (a) and (c) are the top and side views of each model.

to the calculations and E_f of the K^+ intercalation was calculated by a 2 × 2 × 1 supercell. 1–8 K-ions were accommodated between the layers and correspond to x = 0.125–1 in K_xWS_2. In Fig. 5(a), E_f becomes less negative when x is larger than 0.5 (4 K-ions), which indicates a less favorable exothermic reaction between the WS_2 layers and K [42]. Open circuit voltage (OCV) was calculated to estimate the maximum K content (Fig. 5(b)), at which OCV begins to change from positive to negative [43]. The results agree with the E_f calculations, and the maximum K content is between 0.5 and 0.625, corresponding to a maximum intercalation capacity of 54–68 mAh·g^{-1}. Keeping in mind that a significant expansion of the interlayer spacing was observed after discharge, WS_2 monolayer (3 × 3) was applied to the calculations as well to simulate the theoretical upper limit of the K accommodation. 1–10 K-ions were added at two sides of the monolayer and correspond to x = 0.11–1.11 in K_xWS_2. In contrast to bulk WS_2, E_f of monolayer WS_2 (Fig. 5(c)) becomes greatly less negative when x is larger than 0.89 (8 K-ions), and OCV keeps being positive up to x = 1 (Fig. 5(d)), meaning that the maximum capacity can be estimated to be 96–120 mAh·g^{-1}. Atomic structures with different K contents in the two models are shown in Figs. S15 and S16 (in the ESM), respectively. Although the accurate structure of WS_2 during the discharge process is difficult to be simulated at this stage due to the uneven K penetration depth and inhomogeneous K distribution in WS_2, DFT calculations demonstrate the experimental capacity is within the calculated range, and thus verifies the possibility of the intercalation-dominated K^+ storage enabled by the progressive expansion of the interlayer spacing, which accompanies the K intercalation.

3 Conclusions

In summary, we have shown in this work that WS_2 underwent an intercalation-dominated process when inserted by K^+, which is different from the previously reported electrochemical mechanisms of storing K^+ in 2D TMD anodes, where besides an intercalation reaction, a conversion reaction takes place at deep discharge condition. We took advantages of the high reversibility of the intercalation reaction and used WS_2 as a PIB anode. It exhibited low capacity decay rate at both low and high current densities as well as great rate capability. This is the first demonstration of 2D TMDs that serve as an intercalation-type anode in PIBs. We hope this work can shed light on exploring electrochemical ion storage processes that may further our expectations and provide us with insight into material science.

Acknowledgements

This work was supported by the German Research Foundation (DFG: LE 2249/4-1 and LE 2249/5-1). Yuhan Wu would like to acknowledge the China Scholarship Council (CSC) for the financial support.

Electronic Supplementary Material: Supplementary material (experimental details, characterizations of WS_2 powders, CVs, full-cell performance, electrochemical tests of the Na cell, control experiments, calculation of D_k, EIS fitting, and atomic structures of K_xWS_2) is available in the online version of this article at https://doi.org/10.1007/s12274-019-2543-0.

References

[1] Yabuuchi, N.; Kubota, K.; Dahbi, M.; Komaba, S. Research development on sodium-ion batteries. *Chem. Rev.* **2014**, *114*, 11636–11682.

[2] Xu, Y.; Zhou, M.; Lei, Y. Nanoarchitectured array electrodes for rechargeable lithium- and sodium-ion batteries. *Adv. Energy Mater.* **2016**, *6*, 1502514.

[3] Kim, H.; Kim, J. C.; Bianchini, M.; Seo, D. H.; Rodriguez-Garcia, J.; Ceder, G. Recent progress and perspective in electrode materials for K-ion batteries. *Adv. Energy Mater.* **2018**, *8*, 1702384.

[4] Xu, Y.; Zhou, M.; Lei, Y. Organic materials for rechargeable sodium-ion batteries. *Mater. Today* **2018**, *21*, 60–78.

[5] Pramudita, J. C.; Sehrawat, D.; Goonetilleke, D.; Sharma, N. An initial review of the status of electrode materials for potassium-ion batteries. *Adv. Energy Mater.* **2017**, *7*, 1602911.

[6] Zhao, C. L.; Wang, Q. D.; Lu, Y. X.; Li, B. H.; Chen, L. Q.; Hu, Y. S. High-temperature treatment induced carbon anode with ultrahigh Na storage capacity at low-voltage plateau. *Sci. Bull.* **2018**, *63*, 1125–1129.

[7] Guan, D. D.; Yu, Q.; Xu, C.; Tang, C. J.; Zhou, L.; Zhao, D. Y.; Mai, L. Q. Aerosol synthesis of trivalent titanium doped titania/carbon composite microspheres with superior sodium storage performance. *Nano Res.* **2017**, *10*, 4351–4359.

[8] Chen, Z.; Xu, L. H.; Chen, Q.; Hu, P.; Liu, Z. H.; Yu, Q.; Zhu, T.; Liu, H. C.; Hu, G. W.; Zhu, Z. Z. et al. Spray-pyrolysis-assisted synthesis of yolk@shell anatase with rich oxygen vacancies for efficient sodium storage. *J. Mater. Chem. A* **2019**, *7*, 6740–6746.

[9] Eftekhari, A. On the theoretical capacity/energy of lithium batteries and their counterparts. *ACS Sustainable Chem. Eng.* **2019**, *7*, 3684–3687.

[10] Zhang, G.; Liu, H. J.; Qu, J. H.; Li, J. H. Two-dimensional layered MoS_2: Rational design, properties and electrochemical applications. *Energy Environ. Sci.* **2016**, *9*, 1190–1209.

[11] Eftekhari, A. Tungsten dichalcogenides (WS_2, WSe_2, and WTe_2): Materials chemistry and applications. *J. Mater. Chem. A* **2017**, *5*, 18299–18325.

[12] Voiry, D.; Yamaguchi, H., Li, J. W.; Silva, F.; Alves, D. C. B.; Fujita, T.; Chen, M. W.; Asefa, T, Shenoy, V. B.; Eda, G. et al. Enhanced catalytic activity in strained chemically exfoliated WS_2 nanosheets for hydrogen evolution. *Nat. Mater.* **2013**, *12*, 850–855.

[13] Wang, J. B.; Chen, L.; Zeng, L. X.; Wei, Q. H.; Wei, M. D. *In situ* synthesis of WSe_2/CMK-5 nanocomposite for rechargeable lithium-ion batteries with a long-term cycling stability. *ACS Sustainable Chem. Eng.* **2018**, *6*, 4688–4694.

[14] Yu, X. Y.; Prévot, M. S.; Guijarro, N.; Sivula, K. Self-assembled 2D WSe_2 thin films for photoelectrochemical hydrogen production. *Nat. Commun.* **2015**, *5*, 7596.

[15] Taylor, S. R. Abundance of chemical elements in the continental crust: A new table. *Geochim. Cosmochim. Acta* **1964**, *28*, 1273–1285.

[16] Xie, K. Y.; Yuan, K.; Li, X.; Lu, W.; Shen, C.; Liang, C. L.; Vajtai, R.; Ajayan, P.; Wei, B. Q. Superior potassium ion storage via vertical MoS_2 "Nano-rose" with expanded interlayers on graphene. *Small* **2017**, *13*, 1701471.

[17] Lakshmi, V.; Chen, Y.; Mikhaylov, A. A.; Medvedev, A. G.; Sultana, I.; Rahman, M. M.; Lev, O.; Prikhodchenko, P. V.; Glushenkov, A. M. Nanocrystalline SnS_2 coated onto reduced graphene oxide: Demonstrating the feasibility of a non-graphitic anode with sulfide chemistry for potassium-ion batteries. *Chem. Commun.* **2017**, *53*, 8272–8275.

[18] Zhou, J. H.; Wang, L.; Yang, M. Y.; Wu, J. H.; Chen, F. J.; Huang, W. J.; Han, N.; Ye, H. L.; Zhao, F. P.; Li, Y. Y. et al. Hierarchical VS_2 nanosheet assemblies: A universal host material for the reversible storage of alkali metal ions. *Adv. Mater.* **2017**, *29*, 1702061.

[19] Mao, M. L.; Cui, C. Y.; Wu, M. G.; Zhang, M.; Gao, T.; Fan, X. L.; Chen, J.; Wang, T. H.; Ma, J. M.; Wang, C. S. Flexible ReS_2 nanosheets/N-doped carbon nanofibers-based paper as a universal anode for alkali (Li, Na, K) ion battery. *Nano Energy* **2018**, *45*, 346–352.

[20] Ge, J. M.; Fan, L.; Wang, J.; Zhang, Q. F.; Liu, Z. M.; Zhang, E. J.; Liu, Q.; Yu, X. Z.; Lu, B. G. $MoSe_2$/N-doped carbon as anodes for potassium-ion batteries. *Adv. Energy Mater.* **2018**, *8*, 1801477.

[21] Yang, C.; Feng, J. R.; Lv, F.; Zhou, J. H.; Lin, C. F.; Wang, K.; Zhang, Y. L.; Yang, Y.; Wang, W.; Li, J. B. et al. Metallic graphene-like VSe_2 ultrathin nanosheets: Superior potassium-ion storage and their working mechanism. *Adv. Mater.* **2018**, *30*, 1800036.

[22] Ren, X. D.; Zhao, Q.; McCulloch, W. D.; Wu, Y. Y. MoS_2 as a long-life host material for potassium ion intercalation. *Nano Res.* **2017**, *10*, 1313–1321.

[23] Xu, Y.; Bahmani, F.; Zhou, M.; Li, Y. L.; Zhang, C. L.; Liang, F.; Kazemi, S. H.; Kaiser, U.; Meng, G. W.; Lei, Y. Enhancing potassium-ion battery performance by defect and interlayer engineering. *Nanoscale Horiz.* **2019**, *4*, 202–207.

[24] Wang, X.; Huang, J. F.; Li, J. Y.; Cao, L. Y.; Hao, W.; Xu, Z. W.; Kang, Q. Controlling the layered structure of WS_2 nanosheets to promote Na^+ insertion with enhanced Na-ion storage performance. *Electrochim. Acta* **2016**, *222*, 1724–1732.

[25] Von Lim, Y.; Wang, Y.; Kong, D. Z.; Guo, L.; Wong, J. I.; Ang, L. K.; Yang, H. Y. Cubic-shaped WS_2 nanopetals on a prussian blue derived nitrogen-doped carbon nanoporous framework for high performance sodium-ion batteries. *J. Mater. Chem. A* **2017**, *5*, 10406–10415.

[26] Xie, F. Y.; Gong, L.; Liu, X.; Tao, Y. T.; Zhang, W. H.; Chen, S. H.; Meng, H.; Chen, J. XPS studies on surface reduction of tungsten oxide nanowire film by Ar^+ bombardment. *J. Electron Spectros. Relat. Phenom.* **2012**, *185*, 112–118.

[27] Zhang, R. D.; Bao, J. Z.; Pan, Y. L.; Sun, C. F. Highly reversible potassium-ion intercalation in tungsten disulfide. *Chem. Sci.* **2019**, *10*, 2604–2612.

[28] Jeanguillaume, C.; Trebbia, P.; Colliex, C. About the use of electron energy-loss spectroscopy for chemical mapping of thin foils with high spatial resolution. *Ultramicroscopy* **1978**, *3*, 237–242.

[29] Kishore, B.; Venkatesh, G.; Munichandraiah, N. $K_2Ti_4O_9$: A promising anode material for potassium ion batteries. *J. Electrochem. Soc.* **2016**, *163*, A2551–A2554.

[30] Dong, S. Y.; Li, Z. F.; Xing, Z. Y.; Wu, X. Y.; Ji, X. L.; Zhang, X. G. Novel potassium-ion hybrid capacitor based on an anode of $K_2Ti_6O_{13}$ microscaffolds. *ACS Appl. Mater. Interfaces* **2018**, *10*, 15542–15547.

[31] Han, J.; Xu, M. W.; Niu, Y. B.; Li, G. N.; Wang, M. Q.; Zhang, Y.; Jia, M.; Li, C. M. Exploration of $K_2Ti_8O_{17}$ as an anode material for potassium-ion batteries. *Chem. Commun.* **2016**, *52*, 11274–11276.

[32] Deng, L. Q.; Yang, Z.; Tan, L. L.; Zeng, L.; Zhu, Y. J.; Guo, L. Investigation of the prussian blue analog $Co_3[Co(CN)_6]_2$ as an anode material for nonaqueous potassium-ion batteries. *Adv. Mater.* **2018**, *30*, 1802510.

[33] Zhang, C. L.; Xu, Y.; Zhou, M.; Liang, L. Y.; Dong, H. S.; Wu, M. H.; Yang, Y.; Lei, Y. Potassium prussian blue nanoparticles: A low-cost cathode material for potassium-ion batteries. *Adv. Funct. Mater.* **2017**, *27*, 1604307.

[34] Zhou, L. Y.; Yan, S. C.; Pan, L. J.; Wang, X. R.; Wang, Y. Q.; Shi, Y. A scalable sulfuration of WS_2 to improve cyclability and capability of lithium-ion batteries. *Nano Res.* **2016**, *9*, 857–865.

[35] Augustyn, V.; Come, J.; Lowe, M. A.; Kim, J. W.; Taberna, P. L.; Tolbert, S. H.; Abruña, H. D.; Simon, P.; Dunn, B. High-rate electrochemical energy storage through Li^+ intercalation pseudocapacitance. *Nat. Mater.* **2013**, *12*, 518–522.

[36] Lindström, H.; Södergren, S.; Solbrand, A.; Rensmo, H.; Hjelm, J.; Hagfeldt, A.; Lindquist, S. E. Li^+ ion insertion in TiO_2 (anatase). 2. voltammetry on nanoporous films. *J. Phys. Chem. B* **1997**, *101*, 7717–7722.

[37] Zhao, J.; Zou, X. X.; Zhu, Y. J.; Xu, Y. H.; Wang, C. S. Electrochemical intercalation of potassium into graphite. *Adv. Funct. Mater.* **2016**, *26*, 8103–8110.

[38] Xu, Y.; Zhang, C. L.; Zhou, M.; Fu, Q.; Zhao, C. X.; Wu, M. H.; Lei, Y. Highly nitrogen doped carbon nanofibers with superior rate capability and cyclability for potassium ion batteries. *Nat. Commun.* **2018**, *9*, 1720.

[39] Deng, L. Q.; Niu, X. G.; Ma, G. S.; Yang, Z.; Zeng, L.; Zhu, Y. J.; Guo, L. Layered potassium vanadate $K_{0.5}V_2O_5$ as a cathode material for nonaqueous potassium ion batteries. *Adv. Funct. Mater.* **2018**, *28*, 1800670.

[40] Yeh, Y. Y.; Chiang, W. H.; Liu, W. R. Synthesis of few-layer WS_2 by jet cavitation as anode material for lithium ion batteries. *J. Alloys Compd.* **2019**, *775*, 1251–1258.

[41] Xu, Y.; Zhou, M.; Zhang, C. L.; Wang, C. L.; Liang, L. Y.; Fang, Y. G.; Wu, M. H.; Cheng, L.; Lei, Y. Oxygen vacancies: Effective strategy to boost sodium storage of amorphous electrode materials. *Nano Energy* **2017**, *38*, 304–312.

[42] Yu Y. X. Prediction of mobility, enhanced storage capacity, and volume change during sodiation on interlayer-expanded functionalized Ti_3C_2 mxene anode materials for sodium-ion batteries. *J. Phys. Chem. C* **2016**, *120*, 5288–5296.

[43] Er, D. Q.; Li, J. W.; Naguib, M.; Gogotsi, Y.; Shenoy, V. B. Ti_3C_2 mxene as a high capacity electrode material for metal (Li, Na, K, Ca) ion batteries. *ACS Appl. Mater. Interfaces* **2014**, *6*, 11173–11179.